crystals

MDPI

Article

Effects of Ultrasonic Treatment on Grain Refinement and Gas Removal in Magnesium Alloys

Wenyi Hu [1,2,*], Qichi Le [1], Qiyu Liao [1] and Tong Wang [1]

[1] Key Laboratory of Electromagnetic Processing of Materials, Northeastern University, Shenyang 110819, China; liaoliaoqy@mail.neu.edu.cn (Q.L.)
[2] College of Chemistry and Material Science, Longyan University, Longyan 366300, China
* Correspondence: huwenyi@lyun.edu.cn

Abstract: The effects of ultrasonic treatment on grain refinement and hydrogen removal in three kinds of magnesium alloys—Mg-3Ca, Mg-6Zn-1Ca, and AZ80 alloys—were investigated in this study. After ultrasonic treatment, the grains of the magnesium alloys were refined to varying degrees. The degassing effect was characterized by measuring the densities and hydrogen content of ingots. The results indicated that the application of ultrasonic treatment in these magnesium alloys was able to remove hydrogen and obviously refine the microstructure. In this experiment, both the measurement of the density of the ingots and the solid-state hydrogen measurement reflected the degree of degassing. The highest degassing efficiencies were 53.8%, 67.5%, and 34.9% for the Mg-3Ca, Mg-6Zn-1Ca, and AZ80 alloys, respectively. The lowest hydrogen content of the AZ80 alloy reached 8.2 cm^3/100 g, and the corresponding tensile strengths were 174 Mpa, 79 Mpa, and 6.2%, which represented increases of 41.5%, 38.6%, and 87.9%, respectively. The cavitation effect and acoustic streaming effect with an appropriate ultrasonic treatment duration resulted in grain refinement, degassing, and the uniform dispersion of second phases. This can significantly improve mechanical properties and provide a basis for industrial production.

Keywords: ultrasonic field; magnesium alloys; hydrogen content; density of ingot; ultrasonic degassing; cavitation effect

check for updates

Citation: Hu, W.; Le, Q.; Liao, Q.; Wang, T. Effects of Ultrasonic Treatment on Grain Refinement and Gas Removal in Magnesium Alloys. *Crystals* **2024**, *14*, 237. https://doi.org/10.3390/cryst14030237

Academic Editor: Benilde F.O. Costa

Received: 17 November 2023
Revised: 23 January 2024
Accepted: 30 January 2024
Published: 28 February 2024

Copyright: © 2024 by the authors. Licensee MDPI, Basel, Switzerland. This article is an open access article distributed under the terms and conditions of the Creative Commons Attribution (CC BY) license (https://creativecommons.org/licenses/by/4.0/).

1. Introduction

Magnesium alloys have a series of advantages, such as their low density, high specific strength and stiffness, excellent thermal conductivity, electromagnetic shielding performance, damping performance, dimensional stability, and low cost. They are increasingly widely used in the automotive industry, communication electronics industry, aerospace industry, and other fields [1–6].

Currently, casting is the primary method of forming magnesium alloys. However, magnesium alloys absorb a large amount of hydrogen during the melting and casting process. At 730 °C, the solubility of hydrogen is 30 mL/100 g. When hydrogen exceeds the solid solubility limit, the second phase that appears is bubbles, which exacerbate the occurrence of porosity and seriously affect the mechanical and corrosion properties of magnesium alloys [7–10]. Therefore, it is of great significance to reduce the hydrogen content in molten magnesium alloys, but currently, research on this issue is very limited.

High-power ultrasonic waves have unique acoustic effects [11–13]. During the solidification of metals, if appropriate ultrasonic vibration is applied for a certain period of time, the dendritic structure of an ingot will transform from coarse columnar crystals into uniformly fine equiaxed crystals, and both the macro- and microsegregation of the ingot will be improved [14–17]. Ultrasonic waves can effectively remove hydrogen from a melt, thereby improving the compactness of the ingot [18–20]. Currently, the issue of hydrogen removal is mainly considered for aluminum alloys, while hydrogen removal in magnesium alloys is

neglected. In fact, hydrogen removal in magnesium alloys is also important. Traditional methods for hydrogen removal in magnesium alloys include vacuum treatment, inert gas blowing, chlorine gas addition, and rare-earth hydrogen absorption methods. There have been some reports in the literature on ultrasonic hydrogen removal in molten metals, and they mainly focused on aluminum alloys [21–27]. For example, in the Soviet Union [28–30], some researchers found that the mechanism of ultrasonic degassing was intimately attributed to cavitation, which depends on ultrasonic power. An increase in the ultrasonic power could improve the degassing effect. Recently, it was reported by Oak Ridge National Laboratory that the ultrasonic degassing efficiency of A356 alloy melt was related to the ultrasonic treatment's temperature or time. The results indicated that an increase in either temperature or treatment time could improve the degassing effect [31–33]. Wu et al. [34–37] considered that the degassing effect in aluminum alloys in the form of a melt or a semisolid slurry was a combined action of cavitation and ultrasound acoustic streaming, which were related to ultrasonic power. Thus far, studies of hydrogen removal from magnesium alloy melts through ultrasound are seldom found ©n the literature [28,38]. For the purification of magnesium alloy melts, most studies focused on slag removal, while there is very little research on the degassing of magnesium alloys. Therefore, this study focused on several common magnesium alloys, investigated the influence of ultrasonic treatment on hydrogen removal in molten alloys, tested their mechanical properties, and, finally, analyzed the hydrogen removal mechanism. This research can provide a new method and means for the degassing of magnesium alloys and a theoretical basis for industrial production.

2. Experimental Materials and Methods

Figure 1 shows a schematic diagram of the ultrasonic device used in the experiment. The ultrasonic system consisted of a 20 ± 2 kHz ultrasonic generator, a piezoelectric ceramic transducer, a sound emitter, an air-cooling system, and a temperature control system. The power of the ultrasonic generator was adjustable from 0 to 150 W. The temperature of the molten magnesium alloy and the preheating temperature of the ultrasonic emitter were accurately controlled by the temperature control system.

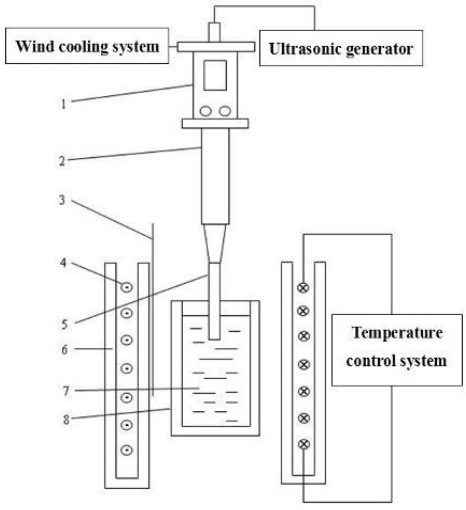


Figure 1. Experiment apparatus of ultrasonic treatment: 1—ultrasonic transducer; 2—amplitude transformer; 3—thermocouple; 4—resistance heater; 5—ultrasonic radiator; 6—ceramic tube; 7—alloy melt; 8—crucible.

Pure industrial magnesium, pure industrial aluminum, pure zinc, and pure calcium were used as raw materials. A Mg-3Ca alloy, Mg-6Zn-1Ca magnesium alloy, and AZ80 industrial magnesium alloy were prepared by melting the materials in an iron crucible. During the melting process, a mixed CO_2 + 0.5% SF_6 gas was used to protect the magnesium alloys from oxidation and combustion. The alloys were heated to 730 °C for complete

melting and then held at 700 °C for 10 min before the ultrasonic treatment. At the same time, the preheated ultrasonic emitter (also at 700 °C) was quickly inserted from the top of the crucible, with the emitter being immersed in the alloy melt to a depth of 10 mm. A constant ultrasonic power of 150 W was applied for a certain period of time, followed by a 10 min holding time. Finally, the treated metal melt (Mg-3Ca and Mg-6Zn-1Ca alloys) was poured into a copper crucible, while the AZ80 magnesium alloy was poured into a water-cooled copper mold. After cooling, the ingots were obtained. The density of the obtained ingots (Mg-3Ca and Mg-6Zn-1Ca magnesium alloys) was measured using the Archimedes method. The ingots were divided into two halves along the longitudinal direction, ground, and polished. Samples of the AZ80 magnesium alloy were taken for hydrogen measurement, microscopic observation of the microstructure, and testing of the mechanical properties. The hydrogen sampling location is shown in Figure 2. The density and hydrogen content of the ingot were measured at least three times. As shown in Figure 2, for the AZ80 alloy, each point was measured three times, and the average value was taken. The samples of the AZ80 alloy were machined into tensile test specimens along the longitudinal direction, and a constant displacement rate of 1 mm/min was applied during the tensile test. A metallographic observation of the three alloys' microstructure was conducted on samples taken from the center of the ingots. A metallographic microscope (Leica DMR, Shanghai, China) and SEM were used for the analysis of the microstructure and phases.

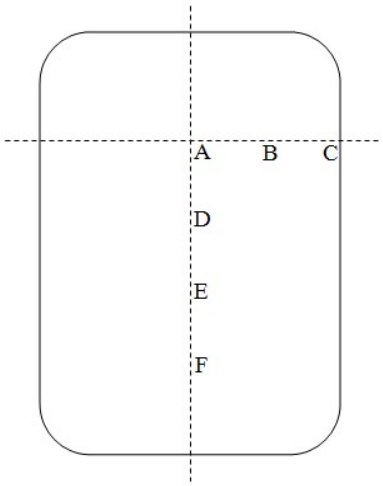


Figure 2. Sampling positions for solid-state hydrogen test.

3. Experiment Results

3.1. Effect of Ultrasonic Treatment on Degassing Efficiency of Mg-3Ca Magnesium Alloy

To evaluate the degassing efficiency, the following definitions were used [23]:

$$\eta_{\text{deg}} = \frac{\rho_a - \rho_0}{\rho_t - \rho_0} \quad (1)$$

ρ_0: Density of the untreated (g·cm^{-3}).
ρ_a: Density of the treated ingot by ultrasonic treatment (g·cm^{-3}).
ρ_t: Theoretical density of the alloy (Mg-3Ca and Mg-6Zn-1Ca have densities of 1.7317 g·cm^{-3} and 1.8183 g·cm^{-3}, respectively).

Figure 3 shows the degassing efficiency of the Mg-3Ca alloy at 700 °C with an ultrasonic power of 150 W for different treatment times. From Figure 3, it can be observed that the degassing efficiency of the alloy increases continuously with increasing in ultrasonic treatment time. The maximum degassing efficiency is achieved at 120 s. However, when the treatment time is extended to 180 s, there is a decreasing trend in the degassing efficiency.

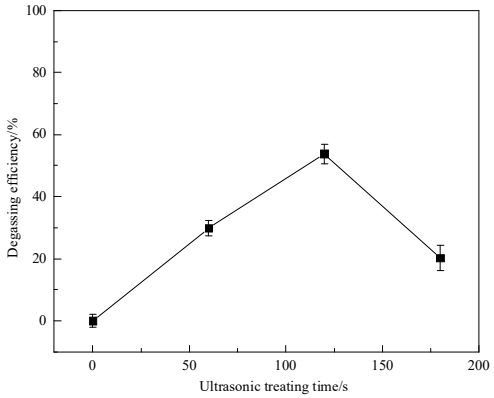


Figure 3. Effect of ultrasonic treating time on degassing efficiency of Mg-3Ca alloy.

Figure 4 illustrates the microstructure of the ingots after different treatment times at 700 °C with an ultrasonic power of 150 W. In the untreated ingot (Figure 4a), the solidification structure of the alloy appears as coarse and uneven dendrites with numerous inter-dendritic pores. After 60 s of ultrasonic treatment (Figure 4b), the grains become more refined and rounded, but a significant number of pores are still visible. When the treatment time reaches 120 s, the grain size slightly coarsens, but the density of the ingot reaches its maximum and the microstructure in the center of the ingot becomes denser. However, as the treatment time is further increased to 180 s, the number of pores in the ingot gradually increases (Figure 4d).

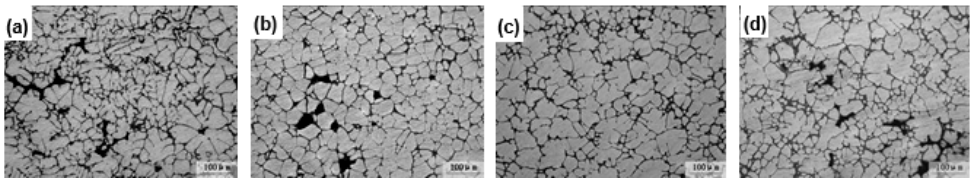


Figure 4. Microstructures of Mg-3Ca alloy treated with different ultrasonic treatment times: (**a**) 0 s; (**b**) 60 s; (**c**) 120 s; (**d**) 180 s.

3.2. The Effect of Ultrasonic Treatment on Degassing Efficiency of Mg-6Zn-1Ca Magnesium Alloy

Figure 5 shows the hydrogen removal efficiency of the Mg-6Zn-1Ca alloy at 700 °C with an ultrasonic power of 150 W for different treatment times. It can be observed that the degassing efficiency of the alloy increases continuously with the ultrasonic treatment time. The maximum degassing efficiency is achieved at 120 s, followed by a decreasing trend in the hydrogen removal efficiency as the treatment time is increased to 150 s.

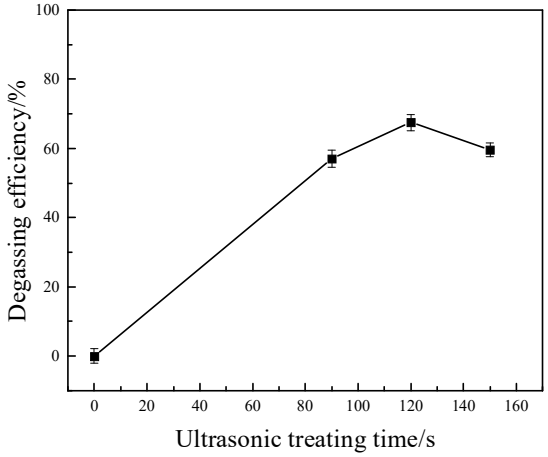


Figure 5. Effect of ultrasonic treatment time on the degassing efficiency of the Mg-6Zn-1Ca alloy.

Figure 6 depicts the microstructure of the ingots after different treatment times at 700 °C with an ultrasonic power of 150 W. The untreated alloy exhibits coarse and uneven grains with numerous intergranular pores, which are commonly observed in the untreated ingots. After 90 s of ultrasonic treatment, the grains become more refined and rounded, but a small number of pores are still present (Figure 6b). When the treatment time reaches 120 s, although the grain size remains the same, the density of the ingot reaches its maximum, and the microstructure in the center of the ingot becomes denser with fewer pores (Figure 6c). However, with a further increase in treatment time, the grain size does not change significantly, but the number of pores and inclusions increases.

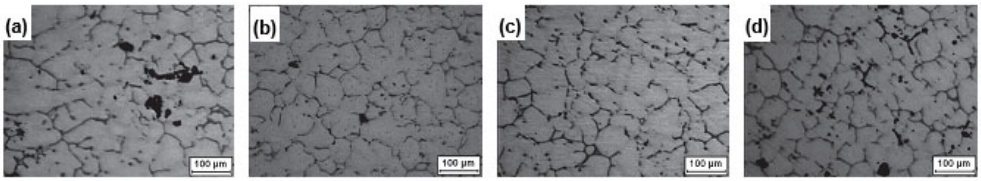


Figure 6. Microstructures of the Mg-6Zn-1Ca alloy treated with different ultrasonic treatment times: (**a**) 0 s; (**b**) 90 s; (**c**) 120 s; (**d**) 150 s.

3.3. The Effect of Ultrasonic Treatment on Degassing Efficiency of AZ80 Magnesium Alloy

In order to characterize the effect of hydrogen removal by hydrogen content, the degassing efficiency is defined as follows:

$$\eta_{\text{deg}} = \frac{C_0 - C}{C_0} \tag{2}$$

where C_0: initial hydrogen content; C: hydrogen content after dehydrogenation.

Figure 7 shows the effect of ultrasonic treatment time on the hydrogen content and degassing efficiency of AZ80 alloy. It can be seen that the hydrogen content in the melt decreases continuously with increasing ultrasonic treatment time. When the treatment time is 90 s, the hydrogen content in the melt can be reduced from 12.6 cm^3/100 g to 8.2 cm^3/100 g. The minimum hydrogen content is 8.2 cm^3/100 g. The degassing efficiency can reach 34.9%. When the ultrasonic treatment time is further increased to 120 s, the degassing efficiency decreases to 25.4%.

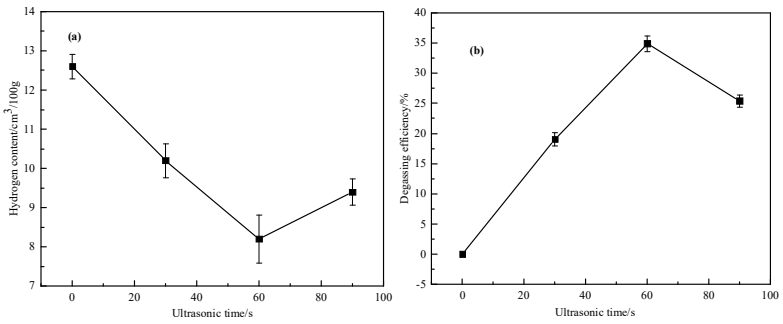


Figure 7. Effect of ultrasonic treating time on hydrogen content and degassing efficiency of the AZ80 alloy: (**a**) hydrogen content; (**b**) degassing efficiency.

Figure 8 is the microstructure photos of AZ80 alloy with different ultrasonic treatment times. It can be seen from the figure that without ultrasonic treatment, the solidification structure is coarse dendrite and there is a little interdendritic porosity and pores, as shown in Figure 8a. After a certain time of ultrasonic treatment, the solidification structure has different degrees of change. When the ultrasonic treatment time is 30 s, 60 s, and 90 s, respectively, the microstructure is fine equiaxed fine grains with uniform distribution, and there are few pores in the microstructure, as shown in Figure 8b–d.

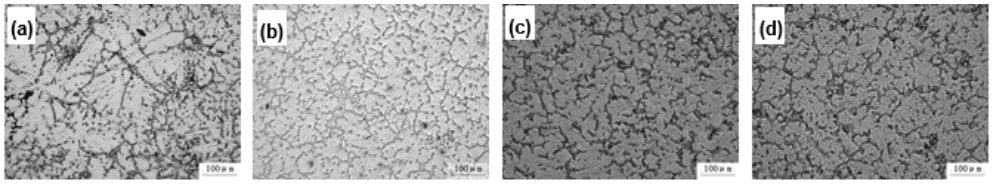


Figure 8. Microstructures of AZ80 alloy treated with different ultrasonic treating time: (**a**) 0 s; (**b**) 30 s; (**c**) 60 s; (**d**) 90 s.

The XRD results showed that the AZ80 alloy was only α-Mg and $Mg_{17}Al_{12}$ phases, as shown in Figure 9. The morphology of the β-$Mg_{17}A1_{12}$ phase directly influences the mechanical properties of the alloy. Figure 10a shows the microstructure of the AZ80 alloy without ultrasonic treatment, which contains a large amount of skeletal or chunky β-$Mg_{17}A1_{12}$ eutectic compounds, mainly distributed in a continuous network pattern along the grain boundaries. After 60 s of ultrasonic treatment, the continuous network of β-$Mg_{17}A1_{12}$ phase becomes discontinuous and finely dispersed.

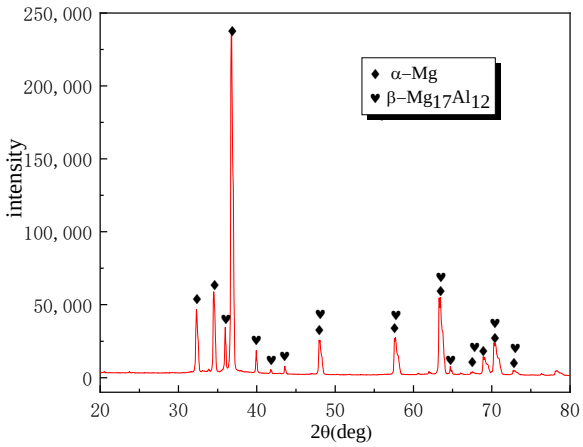


Figure 9. XRD patterns of as-cast AZ80 alloy.

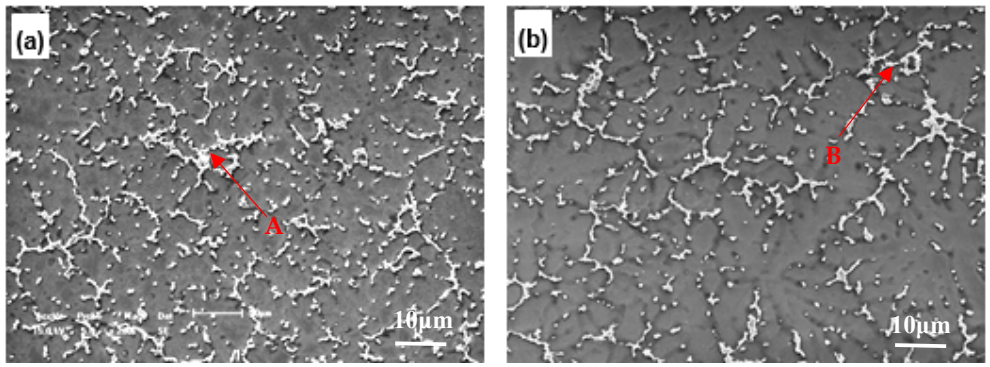


Figure 10. SEM micrographs of AZ80 alloy in the center of samples after ultrasonic treatment: (**a**) 0 s; (**b**) 60 s.

Table 1 presents the EDS results for the phase composition of points A and B.

Table 1. EDS analysis of AZ80 alloy (at.%).

Area	Element (at.%)				Identified Phase
	Mg	Al	Mn	Zn	
A	76.37	22.56	0.02	1.05	β-$Mg_{17}Al_{12}$
B	82.02	14.35	0.03	0.80	β-$Mg_{17}Al_{12}$

Figure 11 indicates the effect of ultrasonic time on the mechanical properties of the AZ80 alloy. The highest tensile strengths were 174 Mpa, 79 Mpa, and 6.2%, which increased by 41.5%, 38.6%, and 87.9% respectively. Figure 12 indicates the SEM pictures of AZ80 alloy treated by different ultrasonic times. The specimen without ultrasonic treatment mainly has brittle fracture. After a certain degree of ultrasonic treatment, a large number of ductile dimples appear on the fracture surface, especially around 60 s to 90 s. However, when the ultrasonic treatment time is too long, the thermal effect of ultrasound causes grain coarsening, resulting in a slight decrease in mechanical properties.

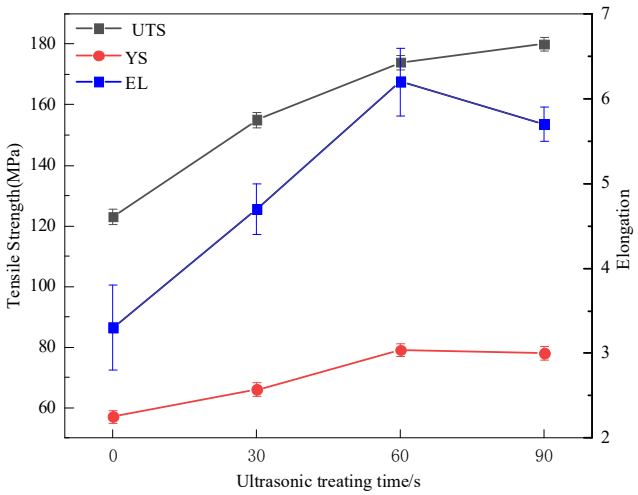


Figure 11. Effect of ultrasonic time on the mechanical properties of the AZ80 alloy.

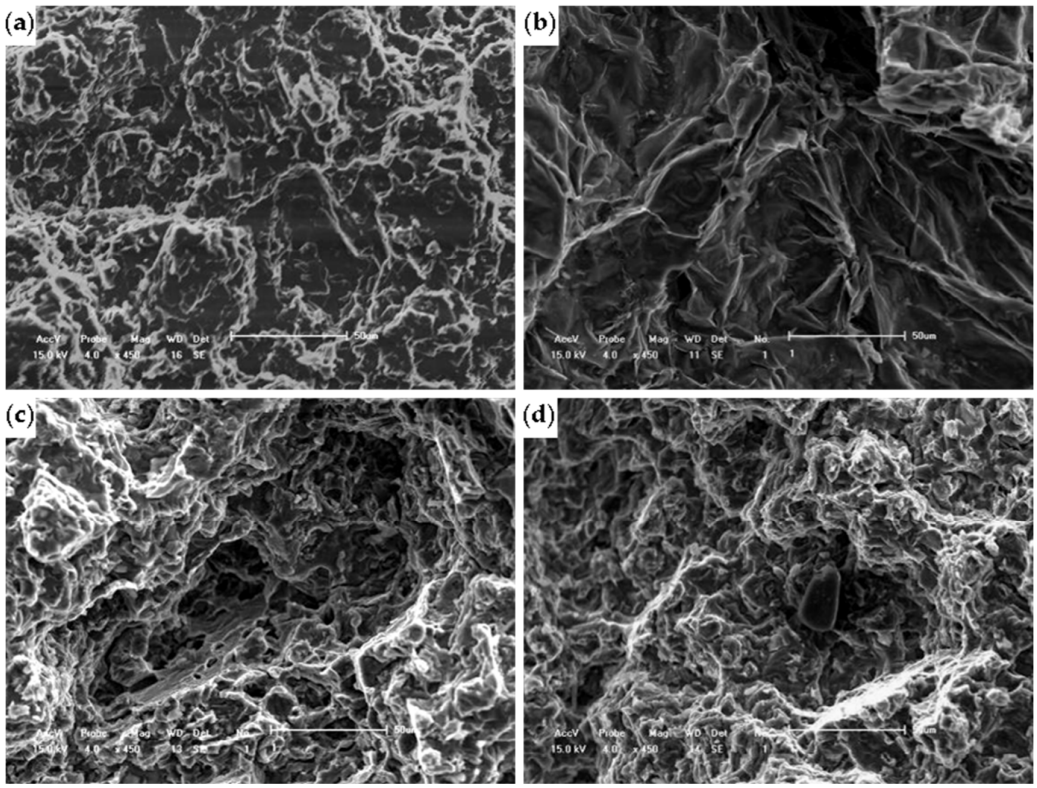


Figure 12. SEM pictures of the AZ80 alloy treated by different ultrasonic times: (**a**) 0 s; (**b**) 30 s; (**c**) 60 s; (**d**) 90 s.

When ultrasonic waves propagate in a liquid, the liquid molecules are subjected to the action of a periodic alternating sound field, resulting in effects such as cavitation

and acoustic streaming, thereby causing changes in the flow field, pressure field, and temperature field in the melt. The cavitation effect of ultrasound is manifested as a series of dynamic processes such as oscillation, growth, shrinkage, and collapse of cavitation bubbles. The collapse of cavitation bubbles generated during ultrasonic cavitation can produce high pressures of about 10^4 MPa (10^5 atmospheres) and temperatures of around 104 °C in their surroundings, with a temperature change rate of up to 10^9 °C/s, which inevitably affects the nucleation and growth of crystals [39,40]. The acoustic streaming effect is due to the finite amplitude attenuation of ultrasonic waves as they propagate in the melt, causing a certain sound pressure gradient to form from the sound source within the liquid, resulting in liquid flow. Stirring the metal melt can improve the uniformity of the temperature field and chemical composition, thereby improving solidification segregation phenomena.

The crystallization of metals is the process of nucleation and growth of crystals. The larger the nucleation rate, the slower the crystal growth rate, and, consequently, the smaller the grain size of the obtained structure. Thus, the grain size depends on the ratio of the nucleation rate to the growth rate, with larger ratios resulting in smaller grain sizes. Factors that promote nucleation and inhibit growth can refine the grains. The specific effects of ultrasonic refinement on the metal crystallization process are reflected in the following aspects: (1) During the transformation of the alloy structure into cellular or dendritic forms, small secondary dendrites and even tertiary dendrites or primary dendrite arms are easily disrupted by the stirring action of ultrasonic waves, and are dispersed throughout the melt with the acoustic streaming formed inside the melt, resulting in the formation of more atomic clusters in the melt. These atomic clusters may collide with each other, causing them to merge or become independent crystallization nuclei, greatly increasing the nucleation rate and promoting grain refinement. (2) When critical crystal nuclei are formed, the surface energy of the crystal nucleus is greater than the volume free energy, and the nucleation resistance is greater than the driving force, requiring additional energy input to nucleate, i.e., work needs to be carried out for nucleation. This nucleation work is the main obstacle during nucleation of undercooled liquid, and the reason why undercooled liquid requires a period of incubation before crystallization begins. The energy required for nucleation work is generally provided by the energy fluctuation and phase fluctuation in the liquid. After introducing ultrasound into the melt, it promotes the early formation of crystal nuclei by inputting energy from the outside, greatly increasing the probability of core nucleation in the melt, thus increasing the nucleation rate. (3) The temperature gradient at the solid–liquid interface has a significant effect on the crystal growth rate. The temperature gradient can be divided into positive and negative temperature gradients. A negative temperature gradient refers to an increase in undercooling with increasing distance to the interface. At this time, the latent heat of crystallization can be dissipated through already-crystallized solid phase and dendrites, or through the as-yet-uncrystallized liquid phase. Most solid solution alloys grow under negative temperature gradients, and their crystallization surfaces are rough interfaces. Due to the large undercooling in the liquid at the front of the interface, if a certain part of the interface develops rapidly and protrudes occasionally, it will extend into the more undercooled liquid, which is more conducive to the growth of this protruding tip into the liquid, forming a primary dendrite. At the same time, the interface between the main dendrite and the surrounding undercooled liquid is also unstable, and many protruding tips will appear on the main dendrite, which will grow into new dendrites, thus forming a dendritic growth pattern. The larger the temperature gradient, the larger the difference in free energy between the solid and liquid phases, and the greater the driving force for crystallization, leading to a higher crystal growth rate. After ultrasonic treatment, strong interaction between acoustic streaming and thermal convection will significantly change the temperature gradient of the melt, visibly improve the uniformity of the temperature field, reduce the temperature gradient, decrease the difference in free energy between the solid and liquid phases, reduce the driving force for crystallization, and slow down the crystal growth rate.

Cavitation and convection action are the driving forces for refining the structure. At a certain melt temperature, as the ultrasonic power increases, the cavitation and convection effects also become stronger, resulting in significant refinement of the structure. However, when the ultrasonic power is relatively high, the thermal effects produced by ultrasound begin to play a very important role, leading to coarsening of the grains. The degree of superheat of the liquid metal has a great influence on nonuniform nucleation. When the superheat is not large, it may not change the surface state of the existing particles, which has no effect on nonuniform nucleation. When the superheat is large, the surface state of some particles' changes, such as the reduction in internal microcracks and small holes in the particles, and the concave surfaces become flat, reducing the number of nonuniform nucleation cores. When the superheat is very large, it causes the solid insoluble particles to melt, leading to a transformation from nonuniform to uniform nucleation, which significantly reduces the nucleation rate. It can be seen that the cavitation and convection effects for refining the structure and the reduction in nucleation rate due to the thermal effects of ultrasound are contradictory. The dominant contradiction determined by the ultrasonic treatment conditions will directly determine the morphology of the structure, such that excessive ultrasonic power leading to thermal effects is detrimental to structural refinement. In order to obtain a good ingot structure, the appropriate ultrasonic treatment time is also crucial for controlling the crystalline structure. This is because after a relatively short period of ultrasonic treatment, a large number of crystal nuclei have not fully formed in the interior of the melt, and the acoustic streaming effect generated during ultrasonic treatment is not sufficient to completely break the already-formed dendrites; hence, the ingot structure cannot be well refined in a short time. On the other hand, if the molten metal is subjected to ultrasonic waves at high power for a long time, a large number of thermal effects will occur, causing the temperature of the molten metal to rise, remelting the previously refined dendrites and coarsening the ingot structure. Therefore, excessively long or short ultrasonic treatment times do not lead to a good refinement of the ingot structure, especially for prolonged high-power ultrasonic treatment, which will result in a noticeable trend of coarsening.

Therefore, when ultrasonic treatment is applied to alloy melts, the liquid molecules are subjected to periodic alternating acoustic fields, causing the liquid to be torn apart by the negative pressure to produce cavitation bubbles. Under the subsequent positive phase of the sound wave, the generated cavitation bubbles close or collapse at extremely high speeds, thus generating instantaneous high pressure, high temperature, and intense shock waves locally in the melt. During the formation and growth process of cavitation, heat is absorbed from the surroundings, which leads to a decrease in the temperature of the metal melt surface area of the cavitation bubble, resulting in localized undercooling. However, during the cavitation bubble collapse process, the strong shock wave generated will break up primary crystals and growing crystals, turning them into shattered crystal particles. The local thermal pulse generated by cavitation continuously impacts the solidification front and causes local melting at the interface. The high temperature generated by cavitation causes dendritic fragmentation and increases nucleation, thereby increasing the number of grains. When the pressure exceeds 10^4 MPa, the transformation from liquid to solid can be achieved. The high pressure generated by ultrasonic treatment exceeds this value, so the acoustic cavitation effect can promote nucleation. Therefore, due to the combined effects of acoustic cavitation and acoustic streaming, the alloy grains become finer and more uniform after ultrasonic treatment. Energy loss occurs during ultrasonic treatment and is absorbed by the melt and converted into heat energy. The longer the treatment time, the more obvious the thermal effect becomes, and the more heat energy is absorbed and converted by the ultrasonic wave in the melt, resulting in a decrease in the cooling rate of the alloy melt and a slowing down of the temperature decrease rate of the melt, leading to an extension of crystal growth time and coarsening of the grains. At the same time, it also breaks up the second phase that is growing, resulting in its fineness and uniformity [41–45].

According to Figure 13, it can be seen that the micropores in the solidified structure of AZ80 are extremely small, only a few micrometers in size, and they are concentrated around the second phase at the grain boundaries.

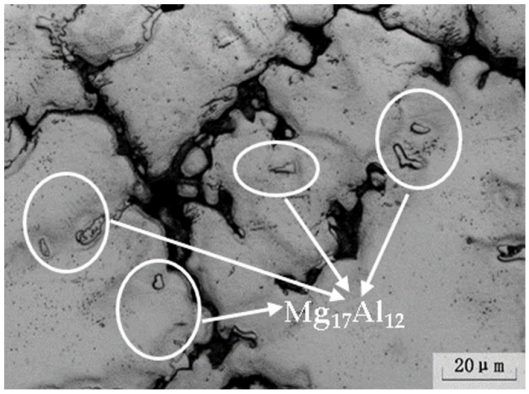


Figure 13. Micropores fracture morphology of AZ80 alloy.

This is related to the fact that the actual solidification process is often nonequilibrium solidification. For the AZ80 alloy, hydrogen in the magnesium melt can be regarded as a solute element similar to Al and Zn. In the actual solidification process (assuming no diffusion in the solid phase and sufficient mixing in the liquid phase), the chemical composition of the first precipitated α-Mg often tends to be lower than the actual composition of the alloy. This is because the solubility of hydrogen decreases rapidly with decreasing temperature, and the first precipitated α-Mg continuously excludes the solute (hydrogen) from its surrounding liquid phase. As the liquid phase is sealed and continues to crystallize, the gas concentration in the remaining liquid phase will continuously increase, and the gas concentration in the subsequent crystallized solid phase will also increase accordingly.

The gas evolution pressure in the liquid and solid phases after solidification continuously increases and reaches its maximum at the end of crystallization. At this time, the micropores formed between dendrites provide conditions for gas evolution, since the pores are in a vacuum state during the initial stage of solidification. The larger the temperature range of crystallization of the alloy (such as AZ80), the earlier the dendrite seals the liquid phase, and the greater the gas concentration in the final solidified liquid phase, resulting in a greater tendency to form these gas pores. In addition, studies have shown that the solubility of hydrogen in the second phase β-$Mg_{17}Al_{12}$ in the alloy is lower than that in magnesium. When the β-$Mg_{17}Al_{12}$ phase precipitates in the liquid phase, it further excludes hydrogen from the remaining liquid phase. These second phases all precipitate at the grain boundaries, and the remaining liquid phase is already very dilute. At this time, hydrogen evolves in the form of hydrogen gas, which coincidentally explains why the micropores often appear near these finally precipitated second phases. The pore formation model is shown in Figure 14.

However, it is unlikely that the micropores observed in Figure 14 are due to insufficient compensation for shrinkage because, typically, voids caused by insufficient compensation for shrinkage are multiple voids clustered together, presenting a cross-sectional profile with different void "arms" in space In addition, hydrogen enriched in the remaining liquid phase also hinders the compensation for shrinkage in the alloy and promotes the formation of shrinkage pores during solidification shrinkage. Therefore, for AZ80 alloy with a wide range of crystallization temperatures, even if the hydrogen content is lower than its solubility, micropores caused by hydrogen evolution can still occur, leading to a reduction in the quality of the castings. Therefore, the hydrogen content must be controlled within a certain range to prevent the occurrence of excessive porosity and discontinuous defects such as gas pores.

Magnesium melt usually contains excessive hydrogen [46,47], most of which has been dissolved in the melt and adsorbed by the inclusions. High-intensity ultrasonic will cause cavitation, i.e., when the alternating sound pressure is negative. When cavitation bubbles frequency and ultrasonic frequency are in resonance [48,49], the cavitation bubbles will obviously grow upwards. The hydrogen atoms in the melt migrate to the gas–liquid interface of the bubble by convection and diffusion, and then hydrogen atoms change from solution to adsorption. The hydrogen atoms which have been adsorbed in the gas–liquid bubble interface mutually coagulate into hydrogen molecules, which diffuse into cavitation bubbles from the gas–liquid interface and become large bubbles, then the hydrogen atoms are removed from the melt surface [50]. Otherwise, tiny bubbles will be moved and have lots of chance of coagulation by means of acoustic streaming. Finally, the bubbles will also float to the liquid level. Therefore, an appropriate ultrasonic treatment time can effectively remove hydrogen from the melt and improve the density of the ingot. When the ultrasonic treatment time is too long and the hydrogen content in the melt is already low, ultrasonic waves, as a disturbance, to some extent tend to increase the entry of external gases into the melt. Therefore, a longer treatment time will result in a higher hydrogen content. In addition, the upward movement of a large number of bubbles in the melt takes a relatively long time. During the casting process, due to the solidification of the ingot, the bubbles cannot be expelled in time and remain inside the ingot, forming pores. In summary, these two factors ultimately lead to a decrease in the density of the ingot and a lower degassing efficiency.

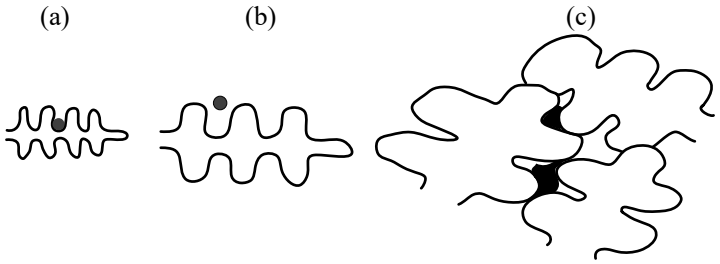


Figure 14. Schematic for microporosity growth [51] (**a**) Hydrogen atoms between dendrites, (**b**) dendrite growth, (**c**) Contact between dendrites seals hydrogen atoms.

4. Conclusions

(1) Appropriate ultrasonic treatment can refine the grain structure and degassing of magnesium alloys, improving the density and degassing efficiency of ingots. The second phases become smaller and more uniform. In these experiments, both density measurement of the ingot and solid-state hydrogen measurement can reflect the degree of degassing. The hydrogen removal effect of Mg-3Ca, Mg-6Zn-1Ca, and AZ80 magnesium alloys was greatly improved by ultrasonic treatment, with maximum hydrogen removal efficiency of 53.8%, 67.5%, and 34.9%, respectively. The effect of ultrasonic treatment on grain size and morphology of $Mg_{17}Al_{12}$ particles in AZ80 alloy was attributed to acoustic cavitation and acoustic streaming.

(2) The lowest hydrogen content of AZ80 magnesium alloy after hydrogen removal can reach 8.2 cm^3/100 g. The corresponding tensile strengths were 174 MPa, 79 MPa, and 6.2%, which increased by 41.5%, 38.6%, and 87.9% respectively. The cavitation effect and acoustic streaming effect with appropriate ultrasonic treatment duration resulted in grain refinement, degassing, and uniform dispersion of second phases. This can significantly improve the mechanical properties and provide a basis for industrial production.

Author Contributions: W.H.: Data curation, writing—original draft. Q.L. (Qichi Le): Investigation, validation, and formal analysis. Q.L. (Qiyu Liao) and T.W.: Resources and methodology. All authors have read and agreed to the published version of the manuscript.

Funding: Open fund of Key Laboratory of Electromagnetic Processing of Materials (No. NEUEPM023), Natural Science Foundation of Fujian Province (No. 2021J05232), Qimai Foundation of Shanghang County (2020SHQM05).

Institutional Review Board Statement: Not applicable.

Informed Consent Statement: Not applicable.

Data Availability Statement: The raw/processed data required to reproduce these findings cannot be shared at this time due to legal or ethical reasons.

Conflicts of Interest: The authors declare no conflicts of interest.

References

1. Jiang, P.; Blawert, C.; Bohlen, J.; Zheludkevich, M.L. Corrosion performance, corrosion fatigue behavior and mechanical integrity of an extruded Mg4Zn0.2Sn alloy. *J. Mater. Sci. Technol.* **2020**, *59*, 107–116. [CrossRef]
2. Pan, H.; Qin, G.; Xu, M.; Fu, H.; Ren, Y.; Pan, F.; Song, B. Enhancing mechanical properties of Mg–Sn alloys by combining addition of Ca and Zn. *Mater. Des.* **2015**, *83*, 736–744. [CrossRef]
3. Boby, A.; Srinivasan, A.; Pillai, U.; Pai, B. Mechanical characterization and corrosion behavior of newly designed Sn and Y added AZ91 alloy. *Mater. Des.* **2015**, *88*, 871–879. [CrossRef]
4. Li, K.; Chen, Z.; Chen, T.; Shao, J.; Liu, C. Hot Deformation and dynamic recrystallization behaviors of Mg-Gd-Zn alloy with LPSO phases. *J. Magnes. Alloys* **2019**, *792*, 894–906. [CrossRef]
5. Chang, L.; Tang, H.; Guo, J. Strengthening effect of nano and micro-sized precipitates in the hot-extruded Mg-5Sn-3Zn alloys with Ca addition. *J. Alloys Compd.* **2017**, *703*, 552–559. [CrossRef]
6. Zhang, Y.; Chen, X.; Lu, Y.; Li, X. Microstructure and mechanical properties of as-extruded Mg-Sn-Zn-Ca alloy with different extrusion ratios. *Trans. Nonferrous Met. Soc. China* **2018**, *28*, 2190–2198. [CrossRef]
7. Zhang, Z.; Le, Q.; Cui, J. Effects of high-intensity ultrasonic on solidification structure of Mg-Ca alloy. *Rare Met. Mater. Eng.* **2008**, *37*, 436–439.
8. Feng, H.; Jia, Z. Effect of C_2Cl_6 on Degassing and Grain Refinement of AZ91 Magnesium Alloy. *Foundry Technol.* **2016**, *37*, 2257–2260.
9. Zhang, Z.; Le, Q.; Cui, J. Microstructures of Mg–Al binary magnesium alloy solidified with ultrasonic treatment. *Mater. Sci. Technol.* **2009**, *25*, 931–934. [CrossRef]
10. Fu, Y.; Li, J.; Song, X. Restraining solute segregation of Al–1%Si alloy in diverse physical field. *Mater. Technol.* **2012**, *27*, 173–175. [CrossRef]
11. Chen, X.; Liao, Q.; Niu, Y.; Jia, Y.; Le, Q.; Ning, S.; Hu, C.; Hu, K.; Yu, F. Comparison study of hot deformation behavior and processing map of AZ80 magnesium alloy casted with and without ultrasonic vibration. *J. Alloys Compd.* **2019**, *803*, 585–596. [CrossRef]
12. Chen, X.; Ning, S.; Wang, A.; Le, Q.; Liao, Q.; Jia, Y.; Cheng, C.; Li, X.; Atrens, A.; Yu, F. Microstructure, mechanical properties and corrosion behavior of quasicrystal-reinforced Mg-Zn-Y alloy subjected to dual-frequency ultrasonic field. *Corros. Sci.* **2020**, *163*, 108289. [CrossRef]
13. Liu, X.; Zhang, J.; Li, H.; Le, Q.; Zhang, Z.; Hu, W.; Bao, L. Electrical resistivity behaviors of liquid Pb-Sn binary alloy in the presence of ultrasonic field. *Ultrasonics* **2015**, *55*, 6–9. [CrossRef]
14. Haghayeghi, R.; Bahai, H.; Kapranos, P. Effect of ultrasonic argon degassing on dissolved hydrogen in aluminium alloy. *Mater. Lett.* **2012**, *82*, 230–232. [CrossRef]
15. Li, J.; Momono, T.; Fu, Y.; Jia, Z.; Tayu, Y. Effect of ultrasonic stirring on temperature distribution and grain refinement in Al-1.65%Si alloy melt. *Trans. Nonferrous Met. Soc. China* **2007**, *17*, 691–697. [CrossRef]
16. Liu, Q.; Zhang, Y.; Song, Y.; Yong, Z. Effects of Power ultrasonic treatment on microstructure and mechanical properties of T10 steel. *Mater. Lett.* **2007**, *61*, 2422–2425. [CrossRef]
17. Helder, P.; Joaquim, B.; Seabra, E.; Ribeiro, S.; Prokic, M. The influence of processing parameters on the ultrasonic degassing of molten AlSi9Cu3 aluminium alloy. *Mater. Lett.* **2009**, *63*, 806–808.
18. Watanabe, T.; Huang, Y.C.; Komatsu, R. Determination of hydrogen content in magnesium. *Light Met.* **1976**, *26*, 67–75. [CrossRef]
19. Watanabe, T.; Tachihara, Y.; Huang, Y.C. The effect of various alloying elements on solubility of hydrogen in magnesium. *Light Met.* **1976**, *26*, 167–174. [CrossRef]
20. Li, J.; Momono, T. Effects of ultrasonic power on refining the crystal structures of ingots and its experimental simulation. *J. Mater. Sci. Technol.* **2005**, *21*, 47–52.
21. Thomson, J.; Liu, P.; Sadayappan, K.; Sadayappan, M. Effect of C_2Cl_6 on mechanical properties and microstructure of gravity permanent mold cast AZ91E. *AFS Trans.* **2004**, 995–1006.
22. Zhang, E.; Wang, G.; Xu, J.; Hu, Z. Grain refinement of AZ91D by spinning spray of carbon dioxide gas and its effect on mechanical property. *Mater. Sci. Technol.* **2010**, *26*, 956–961. [CrossRef]
23. Li, J.; Momono, T.; Yoshinori, T.; Ying, F. Application of ultrasonic treating to degassing of metal ingots. *Mater. Lett.* **2008**, *62*, 4152–4154. [CrossRef]

24. Jun, W.; Ying, F.; Momono, T. Method of fast, effective ultrasonic degassing by forced cooling. *Mater. Res. Innov.* **2010**, *14*, 210–215.
25. Xu, H.; Meek, T.; Han, Q. Effects of ultrasonic field and vacuum on degassing of molten aluminum alloy. *Mater. Lett.* **2007**, *61*, 1246–1250. [CrossRef]
26. Gao, Y.; Wang, Q.; Gu, J.; Tong, Y. Behavior of Mg–15Gd–5Y–0.5Zr alloy during solution heat treatment from 500 to 540 °C. *Mater. Sci. Eng. A* **2007**, *459*, 117–123. [CrossRef]
27. Zhong, G.; Wu, S.S.; Jiang, H.; An, P. Effects of ultrasonic vibration on the iron-containing intermetallic compounds of high silicon aluminum alloy with 2% Fe. *J. Alloys Compd.* **2010**, *492*, 482–487. [CrossRef]
28. Eskin, G. *Ultrasonic Treatment of Light Alloy Melts*; Gordon and Breach Science Publishers: Amsterdam, The Netherlands, 1998.
29. Abramov, O. *High-Intensity Ultrasonics: Theory and Industrial Applications*; Gordon and Breach Science Publishers: London, UK, 1998.
30. Abramov, V.; Abramov, O.; Straumal, B.B.; Gust, W. Hypereutectic Al-Si based alloys with a thixotropic microstructure produced by ultra sonic treatment. *Mater. Design* **1997**, *18*, 323–326. [CrossRef]
31. Xu, H.; Han, Q.; Meek, T. Effects of ultrasonic vibration on degassing of aluminum alloys. *Mater. Sci. Eng. A-Struct.* **2008**, *473*, 96–104. [CrossRef]
32. Jian, X.; Xu, H.; Han, Q. Effect of power ultrasound on solidification of aluminum A356 alloy. *Mater. Lett.* **2005**, *59*, 190–193. [CrossRef]
33. Jian, X.; Meek, T.; Han, Q. Refinement of eutectic silicon phase of aluminum A356 alloy using high-intensity ultrasonic vibration. *Scr. Mater.* **2006**, *54*, 893–896. [CrossRef]
34. Wu, S.; Liu, L.; Ma, Q.; Mao, Y.; Ping, A. Degassing effect of ultrasonic vibration in molten melt and semi-solid slurry of Al-Si alloys. *China Foundry* **2012**, *9*, 201–206.
35. Wu, S.; Lin, C.; Lü, S.; Meng, S. Research progress on microstructure evolution of semi-solid aluminum alloys in ultrasonic field and their rheocasting. *China Foundry* **2014**, *11*, 258–267.
36. Lü, S.; Wu, S.; Dai, W.; An, P.; Mao, Y. Preparation of semi-solid 5052 aluminum alloy slurry by indirect ultrasonic vibration. *Acta Metall. Sin.* **2011**, *47*, 634–640.
37. Wu, S.; Lü, S.; An, P.; Nakae, H. Microstructure and property of rheocasting aluminum-alloy made with indirect ultrasonic vibration process. *Mater. Lett.* **2012**, *73*, 150–153. [CrossRef]
38. He, L.; Li, J. Effect of ultrasonic power on solidification structure and porosity in commercial pure magnesium. *Spec. Cast. Nonferrous Alloys* **2013**, *33*, 182–185.
39. Meidani, A.; Hasan, M. A study of hydrogen bubble growth during ultrasonic degassing of Al-Cu alloy melts. *J. Mater. Process. Technol.* **2004**, *147*, 311–320. [CrossRef]
40. Lin, C.; Wu, S.; Zeng, J.; Ping, A.; Li, W. Combined effects of ultrasonic vibration and manganese on Fe-containing intermetallic compounds and mechanical properties of Al-17Si alloy with 3wt.%Fe. *China Foundry* **2013**, *10*, 148–154.
41. Jia, Z.; Zhang, Z.; Le, Q.; Bao, L.; Cui, J. Effect of ultrasonic melt treatment on degassing of Mg-6Zn-1Ca alloy. *China Foundry* **2015**, *12*, 15–19.
42. Zhao, J.; Ning, L.; Jiang, Z.; Li, Y. Design and Development of a Novel Ultrasonic Field Wetting Angle Measuring Instrument for Researching the Wetting of the Liquid–Solid Interface. *Crystals* **2021**, *11*, 1400. [CrossRef]
43. Zhang, T.; Zhou, J.; Lv, J.; Meng, X.; Li, P.; Huang, S. A novel hybrid ultrasonic and electromagnetic field assisted laser cladding: Experimental study and synergistic effects. *J. Mater. Process. Technol.* **2022**, *307*, 117658. [CrossRef]
44. Wei, Z.; Abolhassan, N.; Morteza, T.; Farzad, S.; Neda, D.; Gholamreza, K. The Effect of an Ultrasonic Field on the Microstructure and Tribological Behavior of ZrB_2/ZrC+Ni60A/WC Composite Coating Applied by Laser Cladding. *Coatings* **2023**, *13*, 1928. [CrossRef]
45. Zhao, S.; Morteza, T.; Kourosh, S.; Mehdi, N.; Khashayar, B.; Moslem, P.; Sai, W. Microstructure of NbMoTaTiNi Refractory High-Entropy Alloy Coating Fabricated by Ultrasonic Field-Assisted Laser Cladding Process. *Coatings* **2023**, *13*, 995. [CrossRef]
46. Hu, Z.; Zhang, E.; Zeng, S. Theoretical analysis and experimental research of degassing of AZ91 magnesium alloy by spinning spraying degassing. *Chin. J. Nonferrous Met.* **2008**, *18*, 1622–1627.
47. Leo, P.; Prasanna, B.; Regener, D. Computational microstructure analyzing technique for quantitative characterization of shrinkage and gas pores in pressure die cast AZ91 magnesium alloys. *CMS* **2005**, *32*, 480–488.
48. Zhang, H.; Zhai, Q.; Qi, F.; Gong, Y. Effect of side transmission of power ultrasonic on structure of AZ81 magnesium alloy. *Trans. Nonferrous Met. Soc. China* **2004**, *14*, 302–305.
49. Liu, X.; Yoshiaki, O.; Susumu, T.; Toshiji, M. Grain refinement of AZ91 alloy by introducing ultrasonic vibration during solidification. *Mater. Lett.* **2007**, *62*, 2872–2875. [CrossRef]
50. Cui, Y.; Xu, C.; Han, Q. Effect of ultrasonic vibration on unmixed zone formation. *Scr. Mater.* **2006**, *55*, 975–978. [CrossRef]
51. Jia, Z. Study on Melts Dehydrogenation Processing of Several Magnesium and Aluminium Alloys. Ph.D. Thesis, Northeastern University, Shenyang, China, 2013.

Disclaimer/Publisher's Note: The statements, opinions and data contained in all publications are solely those of the individual author(s) and contributor(s) and not of MDPI and/or the editor(s). MDPI and/or the editor(s) disclaim responsibility for any injury to people or property resulting from any ideas, methods, instructions or products referred to in the content.